A&A 501, 735–743 (2009)
DOI: 10.1051/0004-6361/200911709

Astronomy & Astrophysics

Acoustic wave propagation in the solar sub-photosphere with localised magnetic field concentration: effect of magnetic tension

S. Shelyag, S. Zharkov, V. Fedun, R. Erdélyi, and M. J. Thompson

Solar Physics and Space Plasma Research Centre, Department of Applied Mathematics, University of Sheffield, Hicks Building, Hounsfield Rd., Sheffield, S7 3RH, UK
e-mail: s.shelyag@sheffield.ac.uk

Received 23 January 2009 / Accepted 4 April 2009

ABSTRACT

Aims. We analyse numerically the propagation and dispersion of acoustic waves in the solar-like sub-photosphere with localised non-uniform magnetic field concentrations, mimicking sunspots with various representative magnetic field configurations.
Methods. Numerical simulations of wave propagation through the solar sub-photosphere with a localised magnetic field concentration are carried out using SAC, which solves the MHD equations for gravitationally stratified plasma. The initial equilibrium density and pressure stratifications are derived from a standard solar model. Acoustic waves are generated by a source located at the height corresponding approximately to the visible surface of the Sun. By means of local helioseismology we analyse the response of vertical velocity at the level corresponding to the visible solar surface to changes induced by magnetic field in the interior.
Results. The results of numerical simulations of acoustic wave propagation and dispersion in the solar sub-photosphere with localised magnetic field concentrations of various types are presented. Time-distance diagrams of the vertical velocity perturbation at the level corresponding to the visible solar surface show that the magnetic field perturbs and scatters acoustic waves and absorbs the acoustic power of the wave packet. For the weakly magnetised case, the effect of magnetic field is mainly thermodynamic, since the magnetic field changes the temperature stratification. However, we observe the signature of slow magnetoacoustic mode, propagating downwards, for the strong magnetic field cases.

Key words. Sun: helioseismology – Sun: magnetic fields – Sun: oscillations – Sun: photosphere – Sun: sunspots

1. Introduction

The internal structure of sunspots remains poorly known. Helioseismological techniques, that analyse the effect of internal solar inhomogeneities on sound wave propagation and the signatures of these waves at the solar surface, might be of great help in revealing the invisible, sub-photospheric solar processes. The ability of forward numerical simulations to predict and model a number of solar phenomena in helioseismology has been shown by e.g., Shelyag et al. (2006), Shelyag et al. (2007), Hanasoge et al. (2007), Parchevsky & Kosovichev (2007), Khomenko et al. (2008), and others. Since magnetic fields are, perhaps, the most important property of many solar features, a new and rapidly developing field is the study of the influence of magnetic fields on the acoustic wave propagation of solar magnetic field concentrations, such as sunspots or solar active regions. The appearance and importance of slow magnetoacoustic waves has been illustrated by forward MHD simulations in polytropic models by Crouch & Cally (2003), Gordovskyy & Jain (2007), Moradi et al. (2009). Ray-approximation simulations in a more realistic and applicable magnetised model have shown a similar behaviour to the acoustic waves (Moradi & Cally 2008). Shelyag et al. (2007) investigated the influence of sub-photospheric flows on acoustic wave propagation using forward modelling and demonstrated a discrepancy between the true flow profiles and the flow profiles obtained by ray-approximation inversion. The simulations of a wave packet, constructed from f-modes, carried out by Cameron et al. (2008), showed a good agreement with helioseismological observations of sunspots.

It is now timely to perform a full forward magneto-hydrodynamic simulation of a wave packet propagating through a non-uniform magnetic field region in the solar sub-photosphere with a realistic temperature profile. Since we are mostly interested in the processes in the solar interior in this paper, we concentrate mainly on the sub-photospheric part of the Sun and do not include the effects of the wave interaction with the solar atmosphere. In the simulations presented here, we consider three different representative configurations of the solar magnetic field. Each case has the common feature of a spatially localised field, allowing direct comparison of both travel speed and time difference of the wave propagation for the magnetised and non-magnetised solar plasma. The representative configurations differ in both magnetic field strength and geometry. Their spatial structure affects the temperature stratification of the simulated sunspot by the magnetic tension. We selected two representative strong field configurations with opposite effects on the temperature in the sunspot: one, where the magnetic field curvature is strong and, thus, increases the temperature in the magnetic field region; and another, where the magnetic field curvature is small, and the temperature is lower in the sunspot. The magnetic configurations that we apply are in magnetohydrostatic equilibrium with the ambient external plasma. These two-dimensional magnetic fields are self-similar and non-potential.

The paper is organised as follows. Section 2 briefly describes the numerical techniques that we used to carry out the simulations. The configurations of the magnetic fields and initial configuration for the simulations are described in Sect. 3.

The source used to generate the acoustic modes in the numerical domain is presented in Sect. 4. Section 5 is devoted to (i) the techniques of helioseismological analysis we used; and (ii) the results we obtained. Section 6 presents our conclusions.

2. Simulation model

The code SAC (Sheffield Advanced Code) was developed by Shelyag et al. (2008) to carry out numerical studies. The code is based on VAC (Versatile Advection Code, Tóth et al. 1998), although, it employs artificial diffusivity and resistivity stabilising the numerical solutions. SAC also uses the technique of variable separation to background and perturbed components to treat gravitationally stratified plasma. According to Shelyag et al. (2008), if a plasma is assumed to be in magnetohydrostatic equilibrium given by

$$(\boldsymbol{B}_b \cdot \nabla)\,\boldsymbol{B}_b + \nabla\frac{\boldsymbol{B}_b^2}{2} + \nabla p_b = \rho_b \boldsymbol{g}, \tag{1}$$

the system of MHD equations governing arbitrary perturbations of density, momentum, energy, and magnetic field is written as

$$\frac{\partial\tilde{\rho}}{\partial t} + \nabla\cdot\left[\boldsymbol{v}\left(\rho_b+\tilde{\rho}\right)\right] = 0 + D_\rho\left(\tilde{\rho}\right), \tag{2}$$

$$\frac{\partial[(\rho_b+\tilde{\rho})\,\boldsymbol{v}]}{\partial t} + \nabla\cdot\left[\boldsymbol{v}\left(\rho_b+\tilde{\rho}\right)\boldsymbol{v} - \tilde{\boldsymbol{B}}\tilde{\boldsymbol{B}}\right] - \nabla\cdot\left[\tilde{\boldsymbol{B}}\boldsymbol{B}_b + \boldsymbol{B}_b\tilde{\boldsymbol{B}}\right] + \nabla\tilde{p}_t = \tilde{\rho}\boldsymbol{g} + \boldsymbol{D}_{\rho v}\left(\left(\tilde{\rho}+\rho_b\right)\boldsymbol{v}\right), \tag{3}$$

$$\frac{\partial\tilde{e}}{\partial t} + \nabla\cdot\left[\boldsymbol{v}\left(\tilde{e}+e_b\right) - \tilde{\boldsymbol{B}}\tilde{\boldsymbol{B}}\cdot\boldsymbol{v} + \boldsymbol{v}\tilde{p}_t\right] - \nabla\cdot\left[\left(\tilde{\boldsymbol{B}}\boldsymbol{B}_b + \boldsymbol{B}_b\tilde{\boldsymbol{B}}\right)\cdot\boldsymbol{v}\right] + p_{tb}\nabla\boldsymbol{v} - \boldsymbol{B}_b\boldsymbol{B}_b\nabla\boldsymbol{v} = \tilde{\rho}\boldsymbol{g}\cdot\boldsymbol{v} + D_e\left(\tilde{e}\right), \tag{4}$$

$$\frac{\partial\tilde{\boldsymbol{B}}}{\partial t} + \nabla\cdot\left[\boldsymbol{v}(\tilde{\boldsymbol{B}}+\boldsymbol{B}_b) - (\tilde{\boldsymbol{B}}+\boldsymbol{B}_b)\boldsymbol{v}\right] = 0 + \boldsymbol{D}_B\left(\tilde{\boldsymbol{B}}\right), \tag{5}$$

where $\tilde{\rho}$ and ρ_b are the perturbation and background density counterparts, respectively, $\boldsymbol{v}$ is the total velocity vector, e_b is the total background energy density per unit volume, $\tilde{e}$ is the perturbed energy density per unit volume, $\boldsymbol{B}_b$ and $\tilde{\boldsymbol{B}}$ are the background and perturbed magnetic field vectors, respectively, $p_{\rm tb}$ is the total (magnetic + kinetic) background pressure, γ is the adiabatic gas index, $\boldsymbol{g}$ is the external gravitational field vector, and $\tilde{p}_t$ is the perturbation to the total pressure

$$\tilde{p}_t = \tilde{p}_k + \frac{\tilde{\boldsymbol{B}}^2}{2} + \boldsymbol{B}_b\cdot\tilde{\boldsymbol{B}}, \tag{6}$$

or, in terms of perturbed energy density per unit volume $\tilde{e}$,

$$\tilde{p}_k = (\gamma-1)\left(\tilde{e} - \frac{(\rho_b+\tilde{\rho})\,\boldsymbol{v}^2}{2} - \boldsymbol{B}_b\cdot\tilde{\boldsymbol{B}} - \frac{\tilde{\boldsymbol{B}}^2}{2}\right), \tag{7}$$

and

$$\tilde{p}_t = (\gamma-1)\left[\tilde{e} - \frac{(\rho_b+\tilde{\rho})\,\boldsymbol{v}^2}{2}\right] - (\gamma-2)\left(\boldsymbol{B}_b\cdot\tilde{\boldsymbol{B}} + \frac{\tilde{\boldsymbol{B}}^2}{2}\right). \tag{8}$$

Here p_{tb} denotes the total background pressure

$$p_{tb} = p_{kb} + \frac{\boldsymbol{B}_b^2}{2}, \tag{9}$$

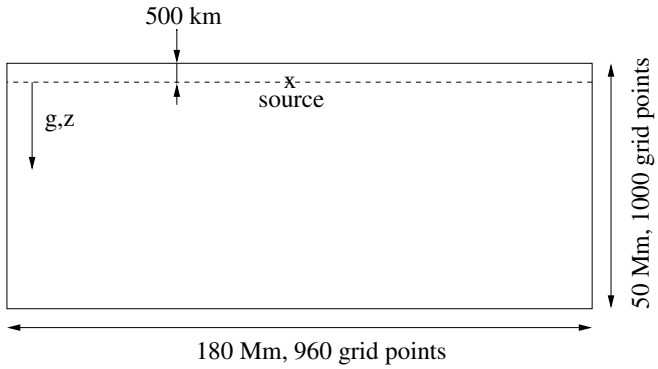

Fig. 1. Sketch of the simulation domain geometry used in the simulations.

which, in terms of background conservative variables, gives

$$p_{kb} = (\gamma-1)\left(e_b - \frac{\boldsymbol{B}_b^2}{2}\right), \tag{10}$$

and

$$p_{tb} = (\gamma-1)\,e_b - (\gamma-2)\,\frac{\boldsymbol{B}_b^2}{2}\cdot \tag{11}$$

The scalar source terms $D_\rho\left(\tilde{\rho}\right)$ and $D_e\left(\tilde{e}\right)$, and the vector source terms $\boldsymbol{D}_{\rho v}\left(\left(\tilde{\rho}+\rho_b\right)\boldsymbol{v}\right)$ and $\boldsymbol{D}_B(\tilde{\boldsymbol{B}})$ on the right-hand sides of the equations denote the artificial diffusivity and resistivity terms. These terms are implemented to stabilise the solution against numerical instabilities, and they are extensively described in e.g., Caunt & Korpi (2001), Vögler et al. (2005), Shelyag et al. (2008), and references therein.

Equations (2)–(11) are solved using a fourth-order central difference scheme for the spatial derivatives and are advanced in time by implementing a fourth order Runge-Kutta numerical method. The simulation domain is shown in Fig. 1. The 2D box is 180 Mm wide and 50 Mm deep, and has a resolution of 960 × 1000 grid points; the upper boundary of the domain is at the solar surface $R = R_\odot$. We employ the simplest type of "open" boundary conditions, assuming that all of the spatial derivatives of the variables, which are advanced in time, are set to be zero across the boundaries of the domain (Caunt & Korpi 2001; Shelyag et al. 2008). The perturbation source is located in the upper-middle (500 km below the upper boundary) of the simulation box. The synthetic measurement level is located at the solar surface.

3. Magnetic fields and initial conditions

For an initial background model, we adopted the Standard Model S (Christensen-Dalsgaard et al. 1996). The model was then adjusted to have the same temperature stratification as the Standard Model, if a constant adiabatic index Γ_1 is assumed. According to the Standard Model S, the pressure at the solar surface $R = R_\odot$ is equal to $p_\odot = 7.61\times10^4$ dyn/cm^2. This provides an upper limit to the vertical uniform magnetic field in magnetohydrostatic equilibrium with non-magnetic external plasma of about $B_{\rm max} = \sqrt{8\pi p_\odot} = 1.4$ kG. The measured magnetic field strength in sunspot umbrae is about 2.5–3.5 kG, which suggests that curved magnetic fields should be implemented in the simulations. In the case of a curved magnetic field, magnetic tension

balances magnetic pressure, thus increasing the upper limit to the equilibrium magnetic field. An example of this balance is a potential magnetic field, where the magnetic tension is exactly equal to the magnetic pressure, and the background pressure and density equilibrium remains unchanged. However, potential magnetic fields can be problematic in numerical modelling. If a potential magnetic field is considered, the boundaries of the numerical domain should be either fixed or periodic to confine the magnetic field and prevent it from strong expansion in the sub-photospheric layers. The sub-photospheric sunspot structure, where the magnetic field is strongly localised, was studied by realistic numerical simulations by Rempel et al. (2009).

We used a self-similar non-potential magnetic field configuration (Schlüter & Temesváry 1958; Schüssler & Rempel 2005; Cameron et al. 2008), which can be obtained from the following set of equations:

$$B_x = -\frac{\partial f}{\partial z} \cdot G(f), \tag{12}$$

$$B_z = \frac{\partial f}{\partial x} \cdot G(f), \tag{13}$$

and

$$f = x \cdot B_{0z}(z), \tag{14}$$

where B_{0z} describes the decrease in the vertical component of magnetic field towards the top of the model, and G is the function defining how the magnetic field opens up with height. The magnetic field constructed in this way is divergence-free by definition. The equilibrium background gas pressure and density are then recalculated using the magnetohydrostatic equilibrium condition in Eq. (1). If the magnetic field $\boldsymbol{B}_b$ is prescribed, Eq. (1) separates into two independent equations for the pressure and density deviations from the initial state, caused by the magnetic field. These equations are then solved numerically to obtain the gravitationally stratified plasma model with a localised magnetic field concentration in magnetohydrostatic equilibrium. The profiles of the functions $B_{0z}(z)$ and $G(x \cdot B_{0z}(z))$ in Eqs. (12)–(14) are shown in Figs. 2 and 3 respectively.

Three characteristic situations, mimicking sunspots that differ in terms of the magnetic field strength at the visible solar surface and curvature of the magnetic field, are chosen for helioseismic analysis: weak but strongly-curved magnetic field ($B_{z,\odot} = 120$ G, Case A), strong but weakly-curved magnetic field with $B_{z,\odot} = 3.5$ kG (Case B), and strongly-curved strong magnetic field ($B_{z,\odot} = 3.5$ kG, Case C). The magnetic field structures for these situations are shown in Figs. 4–6.

The curvature of the magnetic field changes the temperature stratification in the domain. For the first case of the weak magnetic field (Case A, Fig. 4), the temperature change is rather small (Fig. 7). Below the temperature decrease, caused by the sharp decline of the kinetic pressure in the region where the magnetic field is nearly vertical, a temperature increase is noticeable. This increase is caused by the pressure rise needed to compensate for the increase in magnetic tension.

The two initial configurations with strong magnetic field show these processes in greater detail. For Case B (weakly-curved magnetic field, Fig. 4), the temperature is considerably lower beneath the solar surface (Fig. 8), because the magnetic field is nearly vertical at the surface. The effect of magnetic tension is clearly evident in the strongly-curved magnetic field configuration (Case C, Fig. 9). In this latter case, the temperature deviation $\Delta T/T$ is mainly positive.

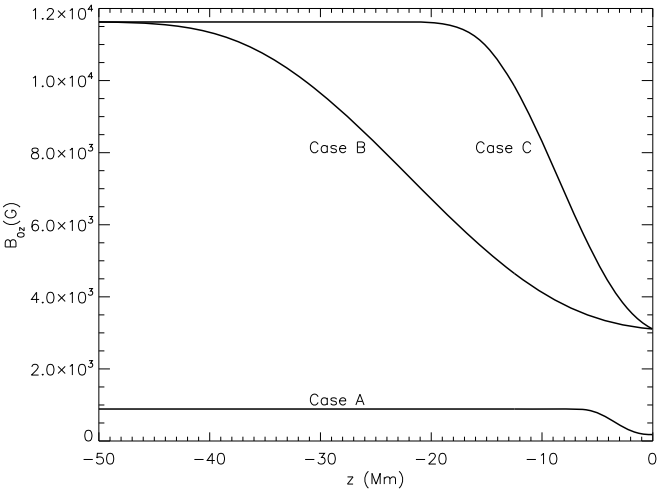

Fig. 2. Vertical magnetic field components on the axis of the magnetic region $B_{0z}(z)$ for the three cases of magnetic field configurations.

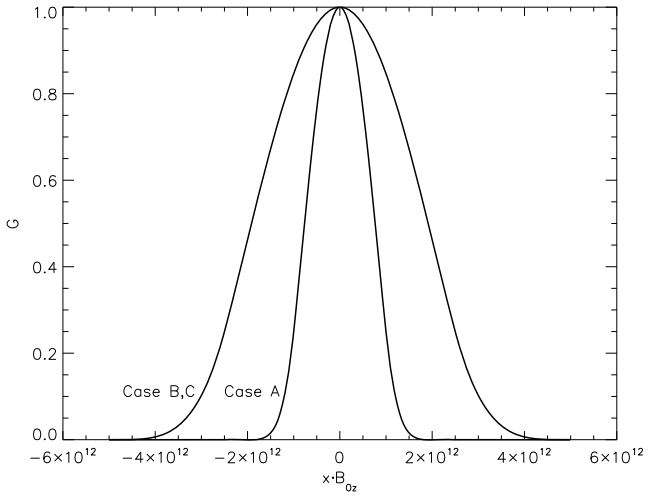

Fig. 3. Functions $G(x \cdot B_{0z}(z))$, used for the calculation of magnetic field for the three different magnetic field configurations.

4. Acoustic source

To generate acoustic waves, we introduce a perturbation source described by the expression

$$v_z = A_0 \sin\frac{2\pi t}{T_0} \exp\left(-\frac{(t-T_1)^2}{\sigma_1^2}\right) \exp\left(-\frac{(r-r_0)^2}{\sigma_0^2}\right), \tag{15}$$

where $T_0 = 300$ s, $T_1 = 600$ s, $\sigma_1 = 100$ s, $\sigma_2 = 0.1$ Mm, and r_0 is the source location. The source is located in the middle of the horizontal layer slightly beneath the solar surface (see Fig. 1). The amplitude of the source A_0 is chosen to be sufficiently small to ensure that convective processes are not initiated in the otherwise convectively unstable equilibrium and the perturbation remains linear, i.e., does not strongly affect the background. The source generates a temporally localised wave packet of duration about 600 s, which has a main frequency of about 3.33 mHz.

The acoustic response of the simulation box to the source is shown in Fig. 10. From the figure, it is evident that the source

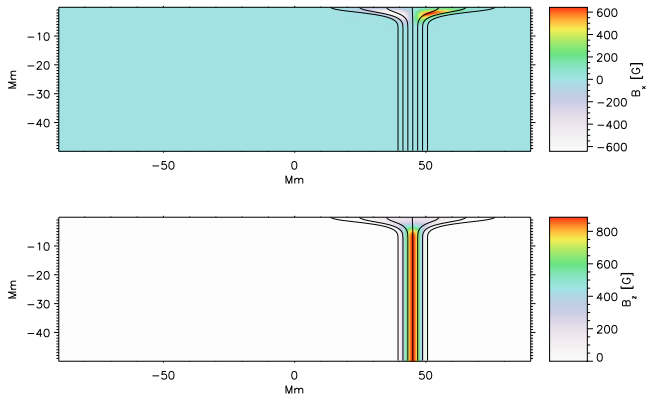

Fig. 4. Magnetic field configuration for a weak magnetic field (Case A) in the sub-photospheric domain of the size of 50 Mm in the vertical and 180 Mm in horizontal direction. The horizontal (B_x) and vertical (B_z) components of the magnetic field are shown. The field lines are overplotted.

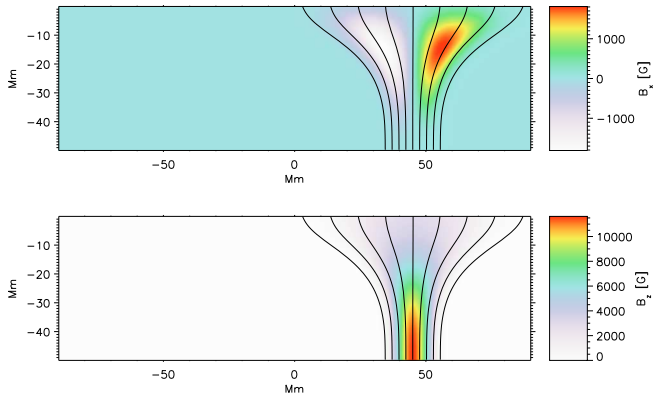

Fig. 5. Same as Fig. 4 with a strong magnetic flux ($B_{z,\odot}$ = 3.5 kG) but weakly-curved magnetic field lines, Case B.

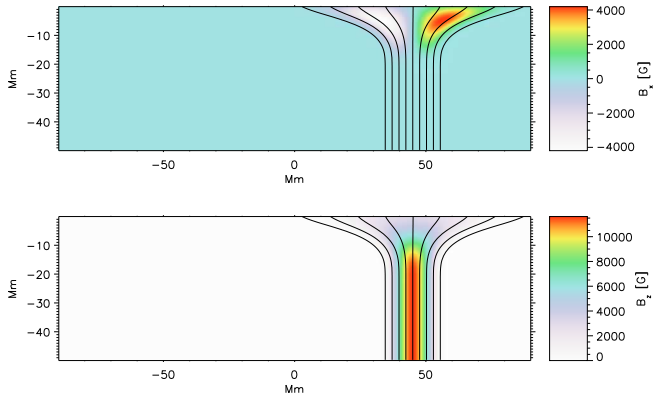

Fig. 6. Same as Fig. 4 with a strongly-curved, strong ($B_{z,\odot}$ = 3.5 kG) magnetic field, Case C.

generates a whole branch of various solar acoustic modes. The p-modes are visible to high order.

To check the validity of the simulations, the one-dimensional calculation of the eigenmodes of the initial background model was also performed. The corresponding eigenfrequencies are overplotted in the figure (solid lines).

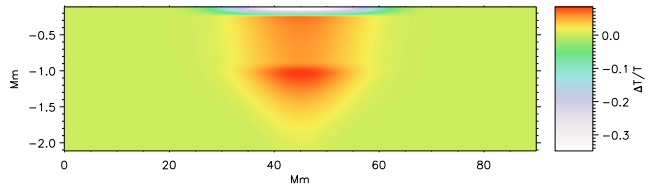

Fig. 7. Zoom-in image of the temperature difference in the magnetic field region for Case A. The temperature increase is caused by magnetic tension.

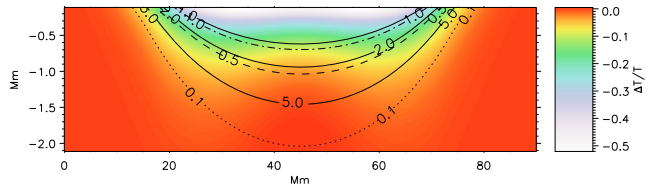

Fig. 8. Same as Fig. 7, with a strong magnetic flux and weakly-curved magnetic field lines, Case B. Here, the temperature decreases at the solar surface. This temperature decrease is caused by magnetic pressure. v_a^2/c_s^2 contours with levels 1, 0.5 and 0.1 (dash-dotted, dashed, and dotted curves), as well as plasma β contours with levels β = 1, 2, 5 (solid curves) are overplotted.

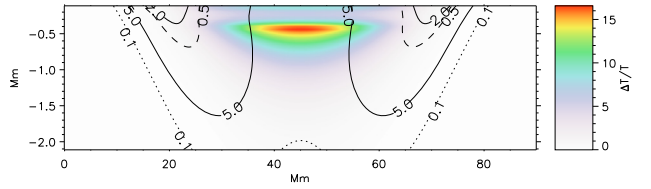

Fig. 9. Same as Fig. 7, with the strongly-curved and strong magnetic field, Case C. In this case magnetic tension prevents evacuation of the magnetic region, and the temperature is increased.

A small difference between the model and the observed solar frequencies is caused by discrepancies between the Standard Model S and the model implemented here, which can be accounted for by using the equation of state for an ideal gas. However, we leave the development of a non-ideal equation of state, including the ionisation processes, and correction of these discrepancies to future work, since they do not play major role in the calculations of the influence of non-uniform magnetic fields on acoustic wave propagation in the solar photosphere.

Figure 11 then shows the time-distance diagram computed at the simulated solar surface by cross-correlating the vertical velocity component, generated by the acoustic source. Three wave bounces are clearly visible on the plot. Some weak and artificial reflection from the side boundaries, caused by imperfectly transparent boundaries of the numerical domain, is also noticeable.

5. Time-distance analysis

As we have mentioned, the acoustic source is located in the middle of the horizontal layer close to the solar surface. This allows us to study the influence of the magnetic field on the acoustic response of the simulated solar sub-photosphere by comparing the plasma velocities to the left (non-magnetic part of the domain) and to the right (where the magnetic field is implemented)

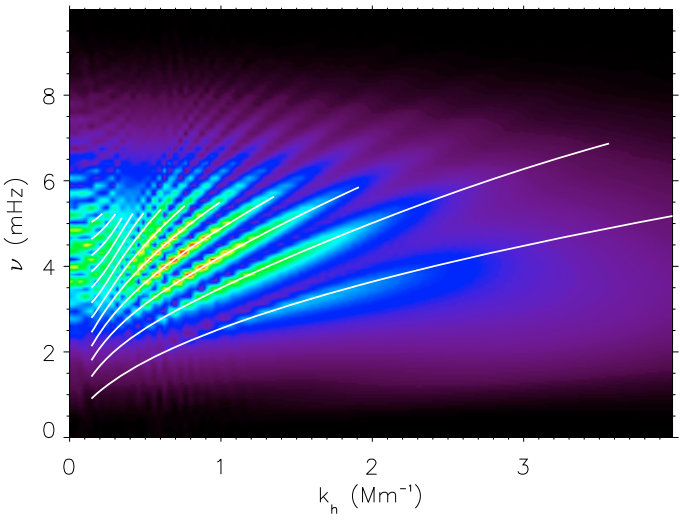

Fig. 10. Power spectrum of the vertical velocity perturbation generated by the source. The *p* modes are visible to high order. Eigenmodes of the background model are overplotted by solid lines.

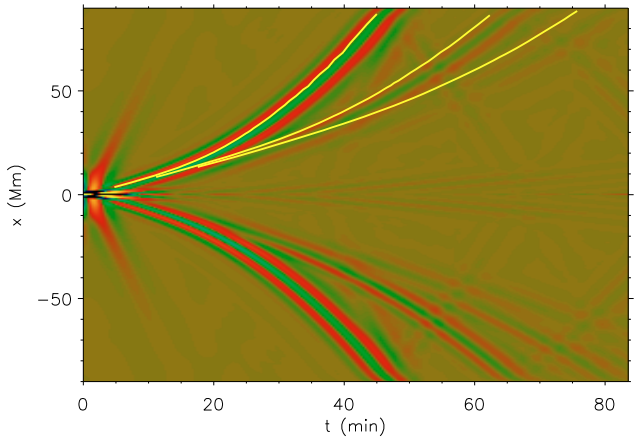

Fig. 11. Cross-correlation function deduced from the vertical velocity perturbation at the solar surface, generated by the acoustic source. Three wave bounces are clearly visible. The group travel times of the first three bounces deduced from ray theory are overplotted.

of the source. A similar technique was proposed and used by Shelyag et al. (2007) to reveal discrepancies between the real and inverted velocity profiles of the sub-photosphere with embedded sub-photospheric horizontal flows.

The vertical velocity differences are computed between the points, located at the same distance to the left and to the right of the source. The difference images, obtained in this way, reveal the phase shifts and amplitude changes the wave packets experience because of the propagation in the magnetised region, compared to propagation in the non-magnetised one.

In magnetic configuration case, we compute the acoustic power of the vertical component of the velocity oscillations over the period of the simulation as a function of horizontal and depth coordinates

$$a_p(x,z) = \int v_z^2(x,z,t)\mathrm{d}t,$$

and then consider the ratio of the corresponding points of the quiet Sun to the perturbed parts of the model. A cut at the surface

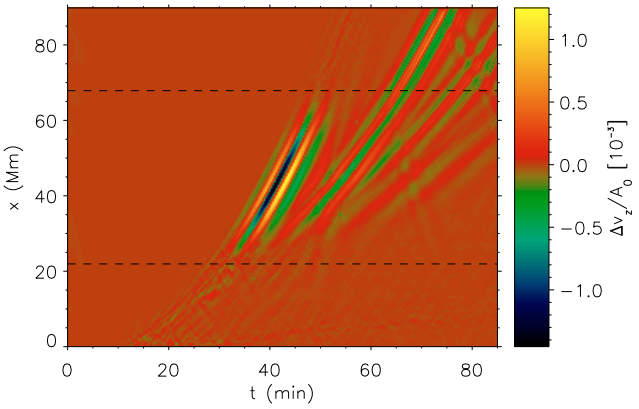

Fig. 12. Vertical speed difference image for Case A. Difference values are computed between points located at the same distance but opposite sides of the source. Two dashed lines bound the magnetic region with $|B| > 25$ G. The first bounce (leftmost in the figure) is affected only locally by the magnetic field, however, the second and third bounces are also affected in the 60–80 Mm distance region.

level corresponds to the acoustic power measurements deduced observationally. In addition, we measured the travel time perturbations by cross-correlating the velocity signal at the source location with the signal at the target location, taking the quiet Sun cross-correlation function as a reference and using both Gábor wavelet fitting (Kosovichev & Duvall 1997) or linearised definition outlined by Gizon & Birch (2002). In Sect. 5.1–5.3, we analyse by these means the wave propagation for the three cases of magnetic field structures. In Sect. 5.4, the results are compared.

5.1. Weak magnetic field (Case A)

The analysis shows that for the configuration of a weak magnetic field (Fig. 4), the influence of the magnetic field on the wave propagation is mainly caused by temperature (and hence local sound speed) changes in the magnetised region. The temperature increase below the simulated sunspot (see Fig. 7) causes negative phase shifts of the wave packets propagating through the magnetic structure.

In Fig. 12, small phase and amplitude changes are observed in all of the bounces, although the first bounce wave is affected only in the magnetic field region (the velocity differences in the figure for the first bounce at 0–30 Mm and at 70–90 Mm are of the order of the numerical noise). It was found that higher order bounces are all affected at a distance of 30 Mm onwards from the source.

In Fig. 13, we present the acoustic power ratio measured in the vertical velocity as a function of two spatial coordinates between the waves propagating in the quiet Sun and in the perturbed part of the model. We found that the power deficit at the location of the flux tube is confined to the uppermost layers of the model with the acoustic power ratio decreasing closer to the surface. The ratio is constant and equal to unity to the left of the flux tube, while to the right we observe variations in the acoustic power at depths of 3 Mm and lower, extending along the straight lines starting below the surface at the flux tube boundary. From the overplotted acoustic rays computed for the unperturbed model, we find that these lines agree well with the envelopes of rays reflected from the simulated solar surface.

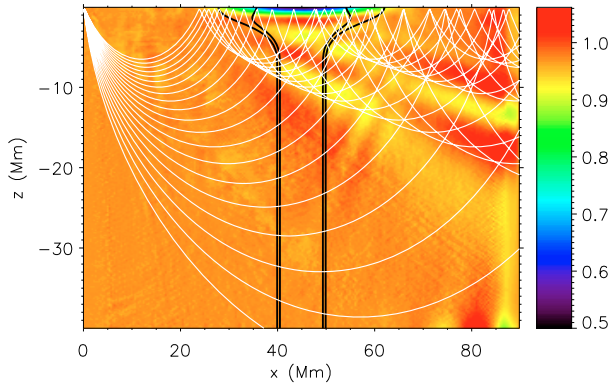

Fig. 13. Synthetic acoustic power ratio image of the weakly magnetised region of the weakly magnetised model (Case A). The ratios are computed between points at the same distance and opposite sides of the source. The image shows the regions of decreased acoustic power compared to the ambient non-magnetic medium. The black lines are the contours of vertical magnetic field at 50 and 100 G, respectively. The acoustic rays for the frequency $f = 3.33$ mHz computed for the quiet Sun model are also overplotted.

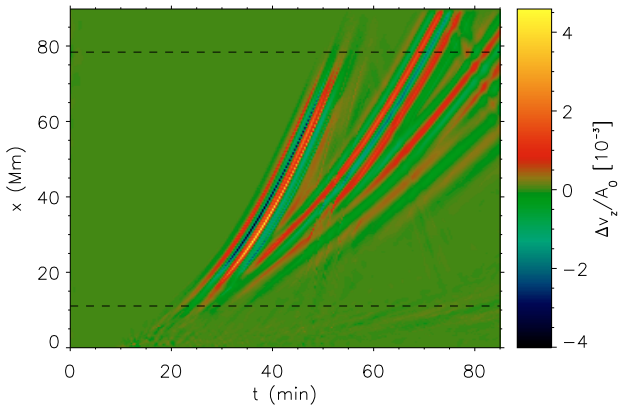

Fig. 14. Same as Fig. 12 but for the strong weakly-curved magnetic field ($B_{z,\odot} = 3.5$ kG), case B. Two dashed lines indicate the magnetic region with $|B| > 250$ G.

5.2. Weakly-curved, strong magnetic field (Case B)

In Case B (see Fig. 5), the temperature distribution is such that the temperature decreases in the sunspot region (Fig. 8), in a way similar to Case A, since the magnetic tension is relatively low. Accordingly to the vertical velocity difference image in Fig. 14, as for Case A, the first bounce is affected by the magnetic field only within the magnetic field region. It is found that the second and higher-order bounces carry information about the interaction with magnetic field also in the non-magnetic or weakly magnetised sub-surface regions. Intuitively, according to the temperature structure, a delay in arrival time of the wave packet at some distance from the source is expected, because the sound speed in the simulated sunspot is lower than in the non-magnetic surrounding plasma. A more detailed analysis confirms this expectation. The first ridge in the image of velocity difference is positive, implying that the wave arrives later at the point in the sunspot than the counterpart wave, which arrives at the same distance in the non-magnetic plasma.

In Case B, the slow magneto-acoustic mode (Cally & Bogdan 1997; Cally 2000; Cameron et al. 2008) is also

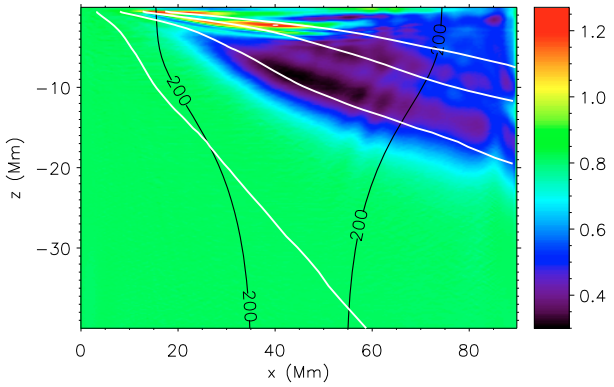

Fig. 15. Total kinetic energy density ratio for the strong magnetic flux but weakly-curved magnetic field lines, Case B. The lower turning points for the first four bounces of rays emanating from the source are overplotted in white. The black lines are the contours of the magnetic field $|B| = 200$ G.

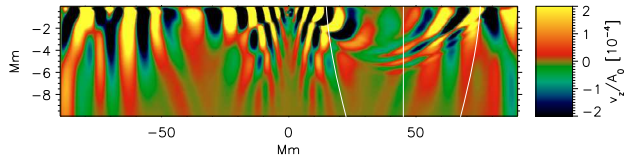

Fig. 16. Snapshot of the horizontal component of the velocity field in the upper layers of the domain, taken at $t = 5130$ s in the simulation for Case B. The slow mode is visible in the magnetised region beneath the solar surface between $x = 20$ Mm and $x = 70$ Mm. The magnetic field lines are overplotted.

observed in the domain (see Fig. 16). Generally, the slow-wave motions follow the magnetic field structure and shape. Furthermore, a suppression of oscillations is observed at the surface in the magnetised region. At a distance of 40 Mm to the right of the source, the amplitude ratio of the horizontal velocity oscillations at the surface to the source amplitude A_0 is about 0.0001, while at the distance of −40 Mm to the left of the source, it is more than 0.0004 (note that the dynamic range of the image has been adjusted so as to enhance the small-amplitude structures). Thus, a significant part of the oscillation energy transforms into slow magnetoacoustic wave motion, which propagates downwards along the magnetic field lines, and is taken out from the surface.

The kinetic energy density ratio plot (Fig. 15) shows the lines of lower ratio, similar to Case A, with the structure immediately below the surface of the tube showing greater complexity than before, perhaps, due to the effect of magnetoacoustic waves. Figure 15 also shows the curves corresponding to lower turning points for the first four bounces of the quiet Sun rays. We note that only the second, third, and fourth bounce turning points correspond to the ray envelopes (see Fig. 13), representing caustic surfaces (Kravtsov & Orlov 1993).

5.3. Strongly-curved, strong magnetic field (Case C)

Strong magnetic tension in Case C (Fig. 6) changes the kinetic gas pressure so that the temperature (and hence sound speed) in the sunspot region increases (see Fig. 9). As expected, the sound speed increase leads to a faster wave propagation through the magnetised region. Correspondingly, the vertical speed

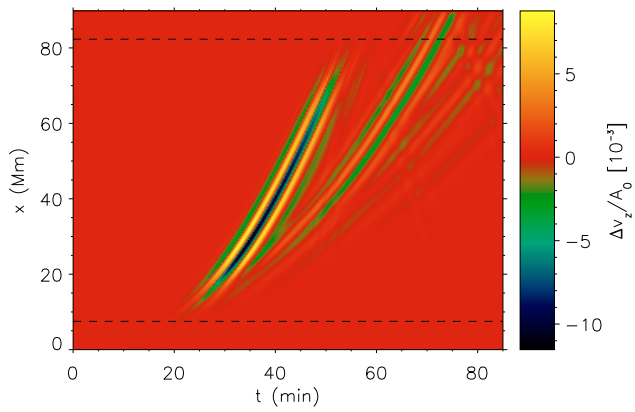

Fig. 17. Same as Fig. 12, but for the strongly-curved, strong magnetic field (Case C). Two dashed lines bound the magnetic region with $|B| > 250$G.

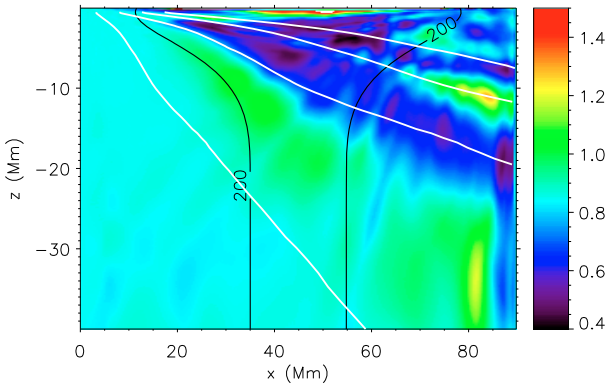

Fig. 18. Oscillatory power in pressure perturbation, scaled by inverse square root of the initial local density ρ_b, for the strongly-curved, strong magnetic field (Case C).

difference image (Fig. 17) has negative sign at the first ridge in the first bounce. Similar to the previous cases, the first bounce is affected by the magnetic field only in the magnetic region (20−70 Mm distance), and the second and higher order bounces are affected everywhere from 20 Mm onwards. We measured the oscillatory power in pressure perturbation, scaled by the inverse square root of the initial local density ρ_b, which is presented in Fig. 18. The same straight line structure as in Cases A and B is observed.

As in the previous case (Fig. 16), the slow magnetoacoustic mode of approximately the same amplitude as in the weakly-curved magnetic field case, is observed in the horizontal velocity component (Fig. 19). Although the true surface $c_s = v_a$ does not appear in the domain, the wave modes remain coupled by the region where the Alfvén speed is close to the sound speed. The presence of a wave of finite wavelength (compared to the ray approximation) suggests that a finite (not infinitely thin) layer exists where the mode conversion occurs, which we observe here. However, the coupling process in this case is less efficient, and the amplitude of the horizontal velocity component in the magnetic region is larger than in the case of a weakly-curved strong magnetic field.

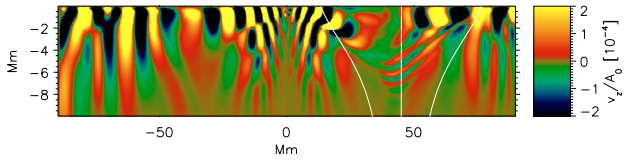

Fig. 19. Same as Fig. 16, for the strongly-curved strong magnetic field, case C. The slow mode is visible between the overplotted magnetic field lines.

5.4. Overall comparison of the effect of magnetic field structures on wave propagation

We have shown that a magnetic field of the same strength acts differently on acoustic waves depending on the geometry and curvature of the field. Here we summarise the findings by showing the travel time difference and wave packet amplitude dependencies for the three representative cases we have analysed.

We have measured the travel time perturbations for the waves travelling through the magnetised region using both a Gabor wavelet method and a method developed by Gizon and Birch. The results for all three different magnetic fields, calculated for the first bounce, are presented in Fig. 20, where the solid lines correspond to Gabor wavelet phase travel-time perturbations and the dashed lines to the travel times defined by Gizon and Birch. We see that the two definitions produce similar results for Cases A and B with small differences that can be explained by the change in the central frequency of the Gabor wavelet (Thompson & Zharkov 2008). In Case C, the significant difference between the two travel time definitions is primarily due to the very large sound speed changes in this model, which practically leads to a non-linear change in measured cross-correlation function, thus breaking one of the assumptions of the definition of Gizon and Birch. The ray travel time perturbations computed for a corresponding hydrodynamic model are overplotted as dash-dotted lines in Fig. 20. These plots clearly show that the sign of travel time differences, calculated for the first bounce, changes according to the temperature difference caused by the magnetic field curvature and tension. The travel time differences obtained for the simulation with the weakly-curved strong magnetic field are of the order of those obtained from the observations (Duvall et al. 1997; Hughes et al. 2005; Zharkov et al. 2007).

Figure 21 illustrates the differences in acoustic power absorption and suppression for the three different magnetic field configurations at the solar surface. The green curve corresponds to Case A. The oscillatory power suppression in the magnetic field region reaches 30%, although, no energy absorption is observed, since the power ratio at the distance $x = 80$ Mm is close to unity. This and the absence of a noticeable slow magnetoacoustic mode in the horizontal component of velocity, confirms our suggestion that the weak magnetic fields act only as temperature and sound speed perturbations for waves propagating through the fields.

The power ratio for Case C (Fig. 21, red curve) significantly differs from that of the other two cases. A very strong suppression of plasma motions in the magnetic field region (up to 90%) is observed. This suppression is caused by the significantly higher temperature of the simulated sunspot. Also, the energy absorption of about 5% is obtained at $x = 80$ Mm. This confirms the partial conversion of the wave packet energy into a slow magnetoacoustic mode, which propagates downwards and removes the energy from the solar surface.

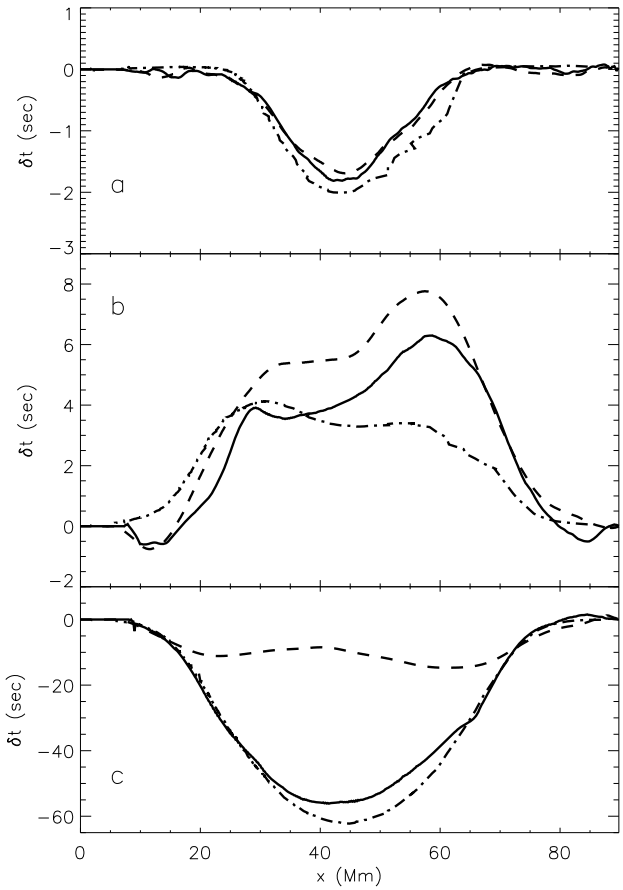

Fig. 20. Travel time difference plots computed for the first bounce for weak (Case A), weakly curved strong (Case B) and strongly curved strong (Case C) magnetic field cases. The solid curves correspond to the travel time perturbations obtained by Gabor wavelet fitting, while the dashed curves represent the travel time perturbations computed using the travel time definition of Gizon and Birch, and dash-dotted curves are the travel time perturbations, calculated using a ray-theoretical approach.

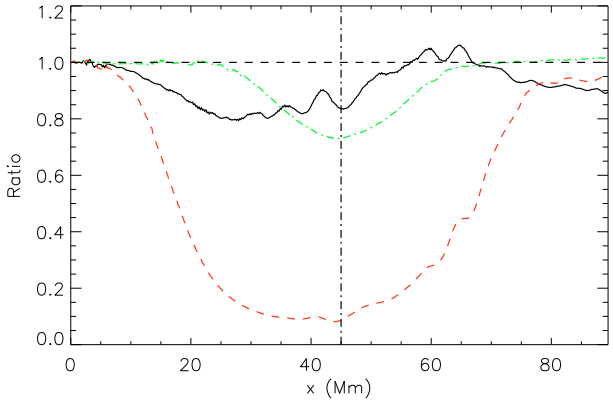

Fig. 21. Acoustic power absorption by the simulated sunspots. The green dash-dotted, black solid and red dashed curves correspond to the case A, case B, and case C magnetic field configurations, respectively. Horizontal dashed line represents the power ratio 1. Vertical dash-dotted line shows the axis of the magnetic configuration.

An even more complicated behaviour is exhibited by the acoustic power ratio at the solar surface, calculated for Case B (Fig. 21, black curve). In this case, the absorption reaches the value of about 10% at $x = 80$ Mm. This seemingly rather low (compared to some observations) absorption coefficient is caused by the different acoustic modes being absorbed differently: while some modes are absorbed strongly and efficiently, other modes are not absorbed at all, and some even can become amplified by the reinforcement due to the mode mixing processes (Cally & Bogdan 1997).

The character of energy suppression in the magnetic field region is also different compared to Cases A and C. The first point here is that the curve is asymmetric with respect to the vertical axis of the magnetic field configuration (note that the green curve, corresponding to the weak magnetic field (Case A) is completely symmetric about the axis, and the red curve is also nearly symmetric, if the energy absorption is not taken into account). We suggest that the wavy structure between $x = 35$ Mm and $x = 50$ Mm is connected to the conversion of purely acoustic wave into slow magnetoacoustic mode. However, the most noticeable feature of this curve is the acoustic power increase of the order of 7–8% at the distance $x = 60$ Mm. This feature is also clearly visible in the two-dimensional power image (Fig. 15), and can be compared with acoustic power haloes around sunspots, which are usually observed (see, for example, the observations by Hill et al. (2001) or Nagashima et al. (2007) and references therein, using the instrument Hinode).

The straight lines emanating at different angles from the flux tube left boundary towards the right edge of the box, visible in both oscillatory power plots of the vertical velocity component, kinetic energy, and pressure perturbation, in our view can be explained in terms of ray theory as caustic surface changes occurring because of the sound-speed inhomogeneity in the x-direction. Caustics corresponding to the envelope of the ray paths for the second and higher-order bounces are approximately co-located with the loci of the lower turning points for the second and higher-order bounces, illustrated in Figs. 13, 15 and 18.

Viewed as the focusing points for the generated waves, the caustics can be characterised by an increase in the oscillation power (Kravtsov & Orlov 1993). Thus, the ratio of the power for the two cases is expected to be most pronounced at these surfaces. This power increase is clearly observed in the time series (movies) of the simulated wave field[1]. The magneto-acoustic mode generation and propagation is also clearly visible in our movies.

6. Conclusions

We have presented numerical modelling and a helioseismological analysis of three physically different, localised magnetic field concentrations, which resemble sunspots in the solar photosphere. The model photosphere is based on the solar standard model S. The acoustic response of this quiet (non-magnetic) solar model is close to that of the real Sun. The magnetic fields implemented in the various simulations differ not only in terms of strength, but also in terms of the curvature of the field lines. The curvature of the magnetic field creates magnetic tension, which consequently changes the pressure, density, and temperature stratification of the equilibrium model. Three representative cases of magnetic fields in equilibrium with the

[1] Available in online material at http://robertus.staff.shef.ac.uk/publications/acoustic/

external non-magnetic photospheric plasma have been considered: weak magnetic field, strong but weakly-curved magnetic field, and strongly-curved but strong magnetic field models. Because of the different magnetic field geometries, different temperature structures were obtained. In the case of a weak magnetic field (Case A), the temperature deviation from the background is small, although there is a complex structure of temperature decrease in the photosphere and temperature increase in the subphotosphere. The two strong magnetic field cases (B and C) have the same magnetic field strength at the surface (3.5 kG). The case of the weakly-curved field (Case B) is characterised by the temperature decrease below the solar surface. However, the strongly-curved magnetic field (Case C) causes a temperature increase there.

The spatial structure of the models that we used to carry out the simulations allows direct and easy comparison of the behaviour of the waves travelling through the non-magnetic plasma with the behaviour of the waves interacting with the magnetic field region. We imposed a magnetic field in only one half of the numerical domain, leaving the other half unaffected by magnetic field.

We analysed the three magnetic field cases by means of local time-distance helioseismology. Synthetic time-distance, time-distance difference, and travel time difference dependencies were calculated from the simulations. The dependencies show that the main effect of the magnetic field on the acoustic wave is caused by the change in the temperature structure in the sunspot. However, we also show that there is an energy leakage downwards in the model due to the wave mode conversion from purely acoustic to slow magneto-acoustic wave motion.

Although the results are intrinsically correct to the order of numerical noise amplitude, we acknowledge that they may have somewhat limited applicability. The simulations were carried out for a magnetic field and background model, which are essentially two-dimensional. Thus, the main applicability limitation of our results is in the energy distribution in the acoustic modes, which is quantitatively (but not qualitatively, if only acoustic and magneto-acoustic waves are considered) different from the three-dimensional case. Also, the absorption of acoustic waves by a magnetic region may in reality differ from the one presented, because of the difference in the acoustic energy distribution. However, since the sound and Alfvén speeds, and the other main magnetohydrodynamic parameters are unaffected by the dimensionality of the problem, the travel times and travel time differences are also independent on the dimensionality. Also, since the upper boundary of the domain is located close to the simulated solar surface, the effects of the interaction of the wave packet with the low-β magnetic field in the solar atmosphere are not taken into account (Schunker & Cally 2006). Consequently, because we expect the large magnetic field influence on the second bounce wave propagation in the solar atmosphere, we limit our travel time difference studies to the first bounce only.

The two-dimensional magnetic fields used in the simulations presented in this paper can be extended to three-dimensional cylindrically symmetric fields. However, simulations of acoustic wave propagation through three-dimensional magnetic structures requires significantly larger computing resources, so we leave this to future analysis.

Acknowledgements. This work was supported by a grant from the UK Science and Technology Facilities Council (STFC). RE acknowledges M. Kéray for patient encouragement. R.E. is also grateful to NSF, Hungary (OTKA, Ref. No. K67746). S. Zharkov acknowledges the support of the HELAS European Network.

References

Cally, P. S. 2000, Sol. Phys., 192, 395
Cally, P. S., & Bogdan, T. J. 1997, ApJ, 486, L67
Cameron, R., Gizon, L., & Duvall, T. L., Jr. 2008, Sol. Phys., 51
Caunt, S. E., & Korpi, M. J. 2001, A&A, 369, 706
Crouch, A. D., & Cally, P. S. 2003, Sol. Phys., 214, 201
Christensen-Dalsgaard, J., et al. 1996, Science, 272, 1286
Duvall, T. L., Jr., Kosovichev, A. G., Scherrer, P. H., et al. 1997, Sol. Phys., 170, 63
Gizon, L., & Birch, A. C. 2002, ApJ, 571, 966
Gordovskyy, M., & Jain, R. 2007, ApJ, 661, 586
Hanasoge, S. M., Duvall, T. L., Jr., & Couvidat, S. 2007, ApJ, 664, 1234
Hill, F., Ladenkov, O., Ehgamberdiev, S., & Chou, D.-Y. 2001, SOHO 10/GONG 2000 Workshop: Helio- and Asteroseismology at the Dawn of the Millennium, 464, 219
Hughes, S. J., Rajaguru, S. P., & Thompson, M. J. 2005, ApJ, 627, 1040
Khomenko, E., Kosovichev, A., Collados, M., Parchevsky, K., & Olshevsky, V. 2008 [arXiv:0809.0278]
Kosovichev, A. G., & Duvall, T. L., Jr. 1997, SCORe'96: Solar Convection and Oscillations and their Relationship, 225, 241
Kravtsov, Y. A., & Orlov, Y. I. (ed.) 1993, Caustics, Catastrophes and Wave Fields (Berlin, GR: Springer-Verlag)
Moradi, H., & Cally, P. S. 2008, Sol. Phys., 251, 309
Moradi, H., Hanasoge, S. M., & Cally, P. S. 2009, ApJ, 690, L72
Nagashima, K., Sekii, T., Kosovichev, A. G., et al. 2007, PASJ, 59, 631
Parchevsky, K. V., & Kosovichev, A. G. 2007, ApJ, 666, 547
Rempel, M., Schüssler, M., & Knölker, M. 2009, ApJ, 691, 640
Schlüter, A., & Temesváry, S. 1958, Electromagnetic Phenomena in Cosmical Physics, 6, 263
Schunker, H., & Cally, P. S. 2006, MNRAS, 372, 551
Schüssler, M., & Rempel, M. 2005, A&A, 441, 337
Shelyag, S., Erdélyi, R., & Thompson, M. J. 2006, ApJ, 651, 576
Shelyag, S., Erdélyi, R., & Thompson, M. J. 2007, A&A, 469, 1101
Shelyag, S., Fedun, V., & Erdélyi, R. 2008, A&A, 486, 655
Thompson, M. J., & Zharkov, S. 2008, Sol. Phys., 251, 225
Tóth, G., Keppens, R., & Botchev, M. A. 1998, A&A, 332, 1159
Vögler, A., Shelyag, S., Schüssler, M., et al. 2005, A&A, 429, 335
Zharkov, S., Nicholas, C. J., & Thompson, M. J. 2007, Astron. Nachr., 328, 240